Geophysical Journal International

Geophys. J. Int. (2021) **224,** 1003–1014
doi: 10.1093/gji/ggaa501
Advance Access publication 2020 October 16
GJI Seismology

Construction of fault geometry by finite-fault inversion of teleseismic data

Kousuke Shimizu ,[1] Yuji Yagi,[2] Ryo Okuwaki [2,3,4] and Yukitoshi Fukahata[5]

[1] *Graduate School of Life and Environmental Sciences, University of Tsukuba, Tsukuba, Ibaraki* 305-8572*, Japan. E-mail: seismo55smz@gmail.com*
[2] *Faculty of Life and Environmental Sciences, University of Tsukuba, Tsukuba, Ibaraki* 305-8572*, Japan*
[3] *Mountain Science Center, University of Tsukuba, Tsukuba, Ibaraki* 305-8572*, Japan*
[4] *COMET, School of Earth and Environment, University of Leeds, Leeds LS*2 9*JT, UK*
[5] *Disaster Prevention Research Institute, Kyoto University, Uji, Kyoto* 611-0011*, Japan*

Accepted 2020 October 13. Received 2020 October 11; in original form 2020 May 7

SUMMARY

Conventional seismic source inversion estimates the earthquake rupture process on an assumed fault plane that is determined *a priori*. It has been a difficult challenge to obtain the fault geometry together with the rupture process by seismic source inversion because of the nonlinearity of the inversion technique. In this study, we propose an inversion method to estimate the fault geometry and the rupture process of an earthquake from teleseismic *P* waveform data, through an elaboration of our previously published finite-fault inversion analysis (Shimizu *et al.* 2020). That method differs from conventional methods by representing slip on a fault plane with five basis double-couple components, expressed by potency density tensors, instead of two double-couple components compatible with the fault direction. Because the slip direction obtained from the potency density tensors should be compatible with the fault direction, we can obtain the fault geometry consistent with the rupture process. In practice we rely on an iterative process, first assuming a flat fault plane and then updating the fault geometry by using the information included in the obtained potency density tensors. In constructing a non-planar model-fault surface, we assume for simplicity that the fault direction changes only in either the strike or the dip direction. After checking the validity of the proposed method through synthetic tests, we applied it to the M_W 7.7 2013 Balochistan, Pakistan, and M_W 7.9 2015 Gorkha, Nepal, earthquakes, which occurred along geometrically complex fault systems. The modelled fault for the Balochistan earthquake is a curved strike-slip fault convex to the south-east, which is consistent with the observed surface ruptures. The modelled fault for the Gorkha earthquake is a reverse fault with a ramp-flat-ramp structure, which is also consistent with the fault geometry derived from geodetic and geological data. These results exhibit that the proposed method works well for constraining fault geometry of an earthquake.

Key words: Image processing; Inverse theory; Waveform inversion; Earthquake dynamics; Earthquake source observations.

1 INTRODUCTION

Earthquakes can rupture fault surfaces with complicated geometry and variable slip vector due to the influence of lithology on fault geometry, the distribution of initial stress, and the dynamic stresses driving the rupture propagation. In mountainous areas, for example, fault geometry tends to be highly non-planar (e.g. Fielding *et al.* 2013; Avouac *et al.* 2014; Elliott *et al.* 2016) due to the typical flats-and-ramps geometry of fold-and-thrust systems (e.g. Elliott *et al.* 2016), which was suggested to introduce spatiotemporal complexities in the regional seismicity (Qiu *et al.* 2016; Dal Zilio *et al.* 2019). It has also been shown that spatial variations in the fault geometry play an important role in rupture propagation (e.g. Aki 1979; Wald & Heaton 1994; Okuwaki & Yagi 2018; Okuwaki *et al.* 2020). Thus, fault geometry has important information that adds detail to our understanding of regional tectonics and earthquake dynamics.

The seismic waveform typically contains information on both rupture propagation and fault geometry underground. Multiple point source inversions have been developed to estimate focal mechanisms and source locations of subevents of large rupture events from seismic waveforms (e.g. Kikuchi & Kanamori 1991; Duputel *et al.* 2012a, b; Duputel & Rivera 2017; Shi *et al.* 2018; Yue & Lay

2020). Although this technique allows us to roughly track rupture propagation from the locations of several point sources, rupture propagation between subevents cannot be well resolved, obscuring the details of rupture propagation and its relationship to fault geometry.

Finite-fault inversion of seismic waveforms has been widely used for resolving rupture propagation in detail along a model fault plane (e.g. Olson & Apsel 1982; Hartzell & Heaton 1983). However, it had been generally difficult to constrain the fault geometry of an earthquake solely by using it because of strong nonlinearity in the inversion analysis (Fukahata & Wright 2008; Asano & Iwata 2009). An inappropriate assumption of fault geometry increases modelling errors, which may greatly distort solutions (e.g. Ragon *et al.* 2018; Shimizu *et al.* 2020).

In a recent paper, we refined the method of Yagi & Fukahata (2011), which explicitly introduced uncertainty of Green's functions into seismic source inversion, to develop a novel method of finite-fault inversion that extracts information on fault geometry as well as rupture propagation from teleseismic *P* waveforms (Shimizu *et al.* 2020). The key to the method is that it adopts five basis double-couple components (Kikuchi & Kanamori 1991), which are not restricted to the two slip components compatible with the fault direction, to represent fault slip. Of course, the true fault geometry should be compatible with the actual slip direction, but because the teleseismic *P*-wave Green's function is insensitive to slight changes in the absolute source location, the new inversion method enables us to infer the spatiotemporal distribution of potency density tensors (e.g. Ampuero & Dahlen 2005) along the assumed model fault plane. Potency density tensors, which are obtained by dividing a moment density tensor by rigidity, contain information on the direction of fault displacement. However, the locations of potency density tensors estimated on an assumed model fault surface can deviate from their true location, which means that the spatial distribution of the strike and dip angles of potency density tensors cannot directly yield the fault geometry. Moreover, the estimated potency density cannot be directly interpreted as slip because the assumed model fault surface is not always identical to the real fault surface. Rupture propagation velocity and its relation to fault geometry are also difficult to properly understand. Thus, source models obtained by the inversion method of Shimizu *et al.* (2020) may not be interpreted in the same way as those obtained by conventional inversion methods, in which a shear slip direction is fixed on the assumed model fault surface.

Here, we propose an iterative inversion method to construct fault geometry from teleseismic *P* waveforms that uses the method of Shimizu *et al.* (2020) to solve the spatial distribution of strike and dip angles on the assumed fault. Iterative solutions allow us to update the fault geometry step by step, yielding a fault geometry that is consistent with the spatial distribution of strike and dip angles. With an improved source model, we can better estimate the relationship between rupture propagation and fault geometry. This paper reports our evaluation of the proposed method through synthetic tests and our successful application of it to waveforms of the M_W 7.7 2013 Balochistan, Pakistan and the M_W 7.9 2015 Gorkha, Nepal, earthquakes, which occurred on well-characterized, geometrically complex fault systems.

2 METHOD

We used the inversion method of Shimizu *et al.* (2020) to construct fault geometries consistent with the spatial distribution of the strike or dip of the obtained potency density tensors. Since the potency density tensors obtained by the inversion method of Shimizu *et al.* (2020) depend to some degree on the assumed model fault geometry, we used the inversion analysis iteratively to construct the fault geometry, at each step solving the spatial distribution of potency density tensors on the assumed fault surface. In this study, we assumed for simplicity that the fault geometry changes only either along strike or along dip and then neglected discontinuity and segmentation of the fault. This assumption leads to two types of model fault: a vertical fault with variable strike and uniform dip direction, and a nonvertical fault with variable dip and uniform strike. The proposed method follows four steps.

Step 1: Set an initial model fault plane

The initial model fault is a single flat plane, which is placed to roughly cover the possible source region of an earthquake (Step 1 in Fig. 1). The model fault is discretized into a number of flat subfaults evenly spaced along the strike and dip directions, with each subfault identical in strike and dip to the model fault plane. The initial rupture point coincides with the earthquake hypocentre obtained from other studies.

Step 2: Perform a potency density tensor inversion

The finite-fault inversion of Shimizu *et al.* (2020) is performed to obtain the spatial distribution of potency density tensors on the initial model fault plane or the non-planar fault surface obtained out of the previous iteration. Displacement of a seismic waveform u_j observed at a far-field station j is represented by a linear combination of potency rate density functions of five basis double-couple components (Kikuchi & Kanamori 1991) on the assumed model fault surface S:

$$u_j(t) = \sum_{q=1}^{5} \int_S G_{qj}(t, \xi) * \dot{D}_q(t, \xi)\mathrm{d}\xi + e_{bj}(t), \tag{1}$$

where G_{qj} is the Green's function of the qth basis double-couple component, $\dot{D}_q$ is the potency rate density function of the qth double-couple component, e_{bj} is background and instrumental noise, ξ represents a location on the model fault surface S, and $*$ is the convolution operator in the time domain. By introducing the modelling error of the Green's function into the inversion analysis (Yagi & Fukahata 2011), the potency rate density function is stably obtained from observed waveforms (Shimizu *et al.* 2020). The spatial distribution of the potency density tensors is obtained by integrating the potency rate density functions with respect to time.

Step 3: Estimate strike/dip along the model fault

In this study, we considered that a fault surface has curvature only along the strike, in which case the fault has a uniform dip, or has curvature only along the dip direction, in which case the fault has a uniform strike. We calculate the average of the estimated potency density tensors along the direction in which the fault is not curved. Thus, for example, along the strike direction of the model fault surface, we obtain focal mechanisms averaged in the dip direction (Step 2 in Fig. 1). To construct a model fault surface, we must select one of the two nodal planes determined by the averaged focal mechanism, which we do for each subfault by calculating the inner product between the normal vectors of the two nodal planes and the normal vector of a reference surface defined by the analyst. In this study, the reference surface is not updated after the first iteration, for simplicity. The nodal plane with the larger inner product (in

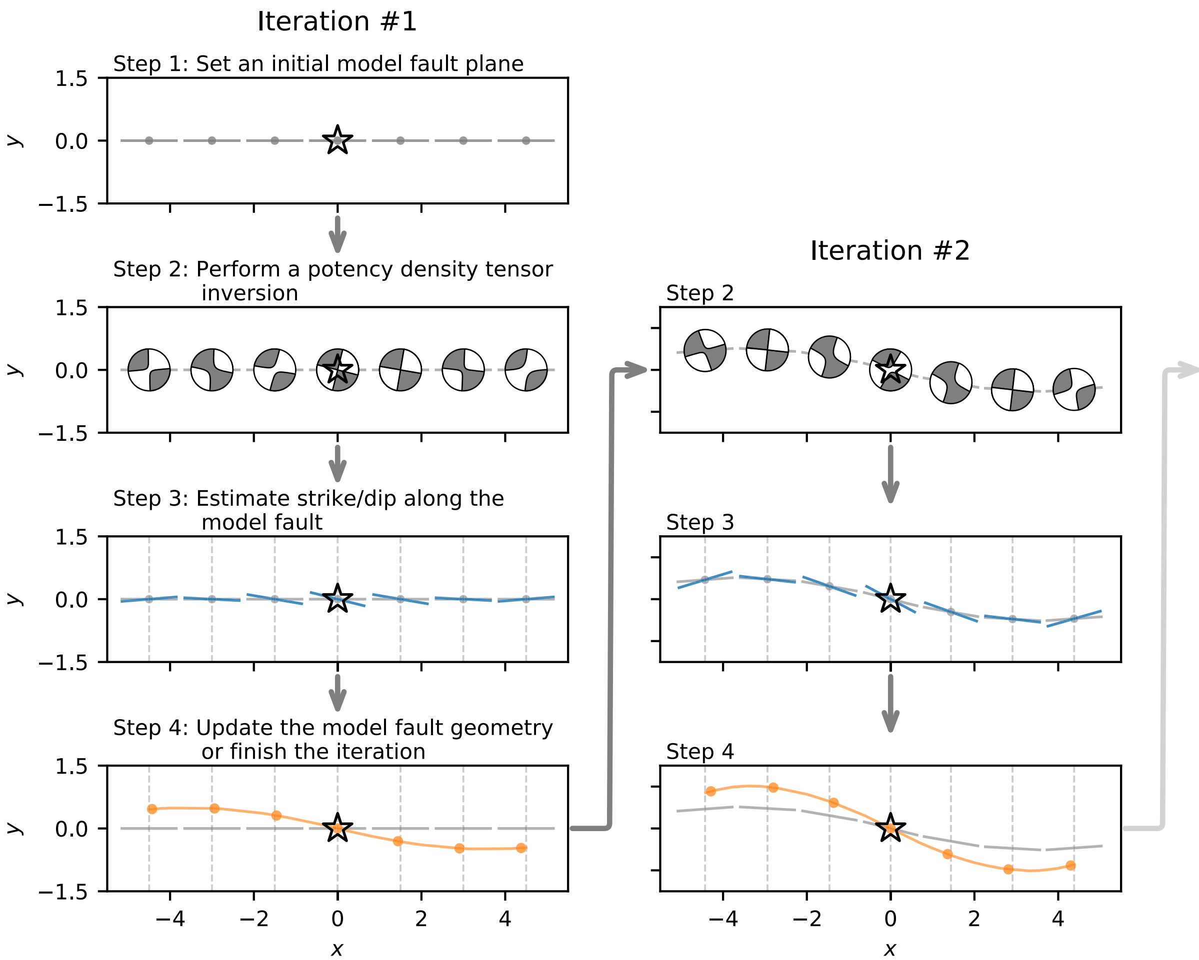

Figure 1. Schematic illustration of the workflow of the iterative inversion process to construct fault geometry. The x axis is the distance from the hypocentre along the strike (or dip) direction of the initial flat model-fault plane. The y axis is the displacement of the updated model fault plane perpendicular to the x axis. The star denotes the location of the hypocentre. Grey bars with grey circles at their midpoints represent subfaults of the model fault plane used in the finite-fault inversion analysis. The beach ball at each subfault in step 2 represents a focal mechanism obtained by the finite-fault inversion of Shimizu *et al.* (2020). In step 3, we select one of the nodal planes (blue line) of the double-couple components to represent the fault geometry from the focal mechanism obtained in step 2. The orange line in the step 4 represents the updated fault geometry determined by spline interpolation with quadratic functions. The orange line of this iteration is used as the model fault geometry in the next iteration.

the absolute) value is selected as the realistic fault plane (Step 3 in Fig. 1).

Step 4: Update the model fault geometry or finish the iteration
Taking the nodal plane selected in step 3 as the direction of the fault surface, we update the fault geometry by assigning the direction of that nodal plane to the centre of each subfault. We smoothly connect the central points of the subfaults by a spline interpolation with a quadratic function f_i:

$$\begin{aligned} y &= f_i(x), \\ f_i(x) &= a_i(x-x_i)^2 + b_i(x-x_i) + c_i \qquad (x_i \le x \le x_{i+1}), \\ i &= 1, 2, \ldots, N-1, \end{aligned} \tag{2}$$

where x is the distance from the hypocentre along the strike/dip direction of the initial flat model plane, y is the displacement of the model fault surface perpendicular to the initial flat model plane, and N is the number of subfaults along the strike/dip. The x_i term, which corresponds to a knot of the quadratic function f_i, is the x coordinate of the central point of the ith subfault along the strike/dip.

Here, the unknown parameters are a_i, b_i, and c_i; the total number of them is $3(N-1)$. The displacement y and its derivative are continuous at the nodes from $i = 2$ to $N-1$:

$$\begin{aligned} f_{i-1}(x_i) &= f_i(x_i), \\ f'_{i-1}(x_i) &= f'_i(x_i), \\ i &= 2, 3, \ldots, N-1. \end{aligned} \tag{3}$$

The number of these conditions is $2(N-2)$. In addition, the gradient of the fault surface at each knot is given by the direction of the nodal plane selected in step 3:

$$\begin{aligned} y'(x_i) &= d_i, \\ i &= 1, 2, \ldots, N, \end{aligned} \tag{4}$$

where d_i represents the gradient of the fault surface at the ith subfault along the strike/dip. The number of this condition is N. Therefore, by fixing the location of the hypocentre (i.e. $f_i(x) = 0$), we can uniquely determine the values of a_i, b_i, and c_i and obtain the updated geometry of the model fault surface (Step 4 in Fig. 1).
After updating the fault geometry, the model fault surface is discretized into rectangular subfaults again. Here, the interval between

central points of adjacent subfaults is taken to be the same as the original one and the distance of the strike/dip direction, to which the fault is bending, is measured not along the original fault strike/dip (the x axis) but along the fault surface. In this study, each subfault is not adjusted to have the same area, which results in slight biases in the estimated density of potency. The model fault surface obtained in step 4 is used to update the fault geometry, and the process returns to step 2 (Fig. 1).

The iterations end when the strike/dip direction obtained by step 3 is sufficiently close to that of the model fault surface used in the inversion analysis. The closeness of the two strikes/dips is based on the inner product between the unit vectors representing the two strikes/dips. When the inner product averaged over the subfaults along the strike/dip is acceptably close to 1 (more than 0.99 in this study), the model fault surface is adopted as the fault surface geometry.

To sum up, the nonlinear inversion method starts from step 1 and then proceeds from step 2 to 4 iteratively. We assign (step 1) or update (step 4) the fault geometry, with which we solve the potency density tensor distribution (step 2), and then extract the information from that solution (step 3) to update the fault geometry (step 4).

3 SYNTHETIC TESTS

We performed synthetic tests of the proposed method for a strike-slip fault (case 1) and a dip-slip fault (case 2). For both cases, we prepared input source models, described below, and calculated synthetic velocity waveforms by using theoretical Green's functions. In both cases, the slip-rate function at each subfault was represented as a combination of linear B-spline functions with a time interval of 0.8 s. Theoretical Green's functions were calculated following the method of Kikuchi & Kanamori (1991) at 0.1 s intervals, where the attenuation time constant t^* for the P wave was taken to be 1.0 s. The 1-D near-source velocity structures for the cases 1 and 2 are listed in Tables S1 and S2 in the Supporting Information, respectively. In the calculation of synthetic waveforms, we added errors of Green's function and background noise to synthetic waveforms. As an error of Green's function, we added random Gaussian noise with zero mean and a standard deviation of 5 per cent, which was arbitrarily chosen rate, of the maximum amplitude of each calculated Green's function. We then added random Gaussian noise with zero mean and a standard deviation of 1 μm as the background noise. In the inversion process, we resampled the calculated synthetic waveform data at 0.8 s intervals without applying any filter to either the calculated waveforms or the theoretical Green's functions.

3.1 Case 1: strike-slip fault with variable strike

We applied the proposed method for a vertical fault with variable strike and uniform dip direction. The fault is composed of two vertical flat fault planes, each one 75 km long and 20 km wide, with strikes of 160° and 200°, respectively (Fig. 2a). The slip distribution of the input source model with two slip patches is shown in Fig. 2(b). The slip direction is pure right lateral. The input slip-rate function at each subfault had a total duration of 6 s. The hypocentre location was 26.900°N, 65.400°E at a depth of 7.5 km. Rupture of each subfault was triggered by the expanding circular rupture front propagating from the hypocentre at 3 km s^{-1}. Synthetic waveforms were calculated for the selected stations shown in Fig. 2(c).

In the inversion analysis, the initial model fault was a vertical plane 150 km long and 20 km wide with a strike of 180° (Fig. 3a). The potency rate density functions on this plane were expanded by bilinear B-spline functions with a spatial interval of 5 km and by linear B-spline functions with a temporal interval of 0.8 s and a total duration of 6 s. The hypocentre was the same one used as the input. The maximum rupture front velocity was assumed to be 3 km s^{-1}. We adopted a plane with a strike of 354° and a dip of 89°, derived from the total potency tensor obtained by a preliminary analysis, as the reference surface used for selecting realistic nodal planes.

The obtained fault model after two iterations reproduced the straight parts and bend in the input fault very well (Fig. 3a). The slip distribution with two slip patches (Fig. 3c) was also consistent with the input source model, including the slip direction (Fig. 2b). Although the distributions of potency density tensors obtained after the first and the last iterations are quite similar to each other (Supporting Information Fig. S5), the source model obtained after the last iteration also reproduced fault geometry of the input source model (Fig. 3a), which can be said to highlight the advancement made in this study. Testing the model's sensitivity to the strike of the initial model plane by changing it to 170° and 190°, we obtained nearly the same results (Figs 3b and c). However, large deviations of the initial fault plane from the true one and the modelling error of the Green's function, which increases with distance from the hypocentre, may cause unstable estimates of fault geometry, as seen at the southern end of the model fault with 170° strike. These results confirm that the proposed method works well for faults with variable strike when the initial model fault plane is reasonably accurate.

3.2 Case 2: reverse fault with variable dip angle

We applied the proposed method for a nonvertical fault with variable dip and uniform strike. The fault is composed of three adjacent planes with different dips (Fig. 4a). The three planes had a 285° strike and together extended 65 km; from top to bottom their dips were 20°, 0° and 20°, and their widths were 20, 25 and 20 km, respectively. The slip distribution of the input source model is shown in Fig. 4(b). The input slip-rate function at each subfault had a total duration of 10 s. The hypocentre location was 28.231°N, 84.731°E at a depth of 15 km. Rupture in each subfault was triggered by the expanding circular rupture front propagating from the hypocentre at 3 km s^{-1}. Synthetic waveforms were calculated for the selected stations shown in Fig. 4(c).

In the inversion analysis, the initial model fault was a horizontal plane 65 km long and 75 km wide, and 15 km deep with a strike of 285° and a dip of 0° (Fig. 5b). The potency rate density functions on this plane were expanded by bilinear B-spline functions with a spatial interval of 5 km and by linear B-spline functions with a temporal interval of 0.8 s and a total duration of 10 s. The hypocentre was the same one used as the input. The maximum rupture front velocity was assumed to be 3.0 km s^{-1}. We adopted a plane with a strike of 273° and a dip of 11°, derived from the total potency tensor obtained by a preliminary analysis, as the reference surface used for selecting realistic nodal planes.

The obtained fault model after two iterations, shown in Fig. 5(a) as a 3-D view and in Fig. 5(b) as a cross sectional view, features a dip that ranges from 4° around the hypocentre to 18° and 19° near the up-dip and down-dip edges, respectively. The obtained fault model reproduced the input fault geometry and its slip distribution well (Fig. 5d), although its geometry was slightly smoother. Testing the model's sensitivity to the dip of the initial model plane by changing it to 10° and 20°, we obtained nearly the same results (Figs 5c and

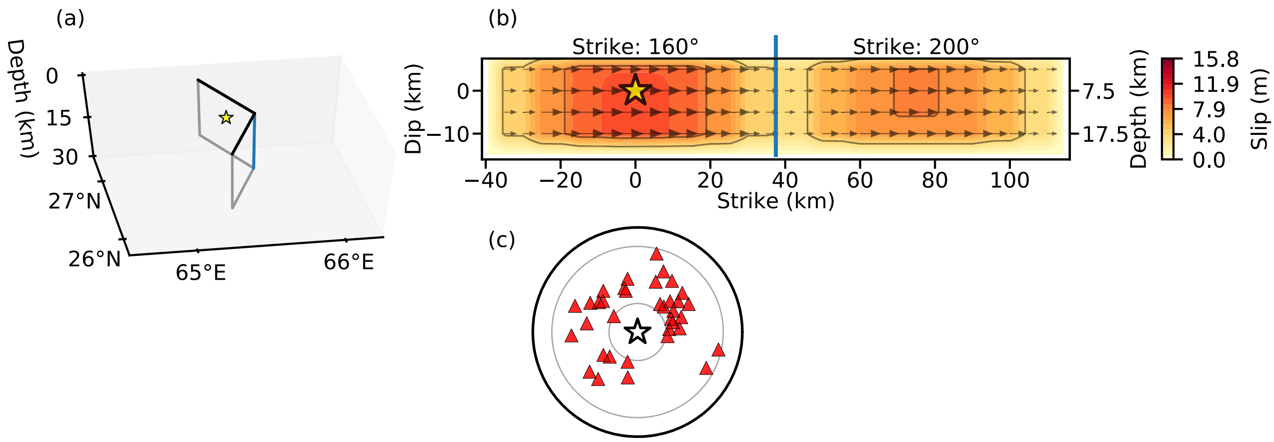

Figure 2. Input source model for case 1. (a) Fault geometry. The input fault plane consists of two vertical rectangles with different strikes that meet the surface along the black lines and intersect on the blue line. The yellow star denotes the hypocentre. (b) Slip distribution on the input fault plane; contour interval is 4 m. The arrows are slip vectors, and the star denotes the hypocentre. (c) Station distribution (red triangles) around the epicentre (star) in an azimuthal equidistant projection. The grey circles indicate the 30° and 90° teleseismic distances.

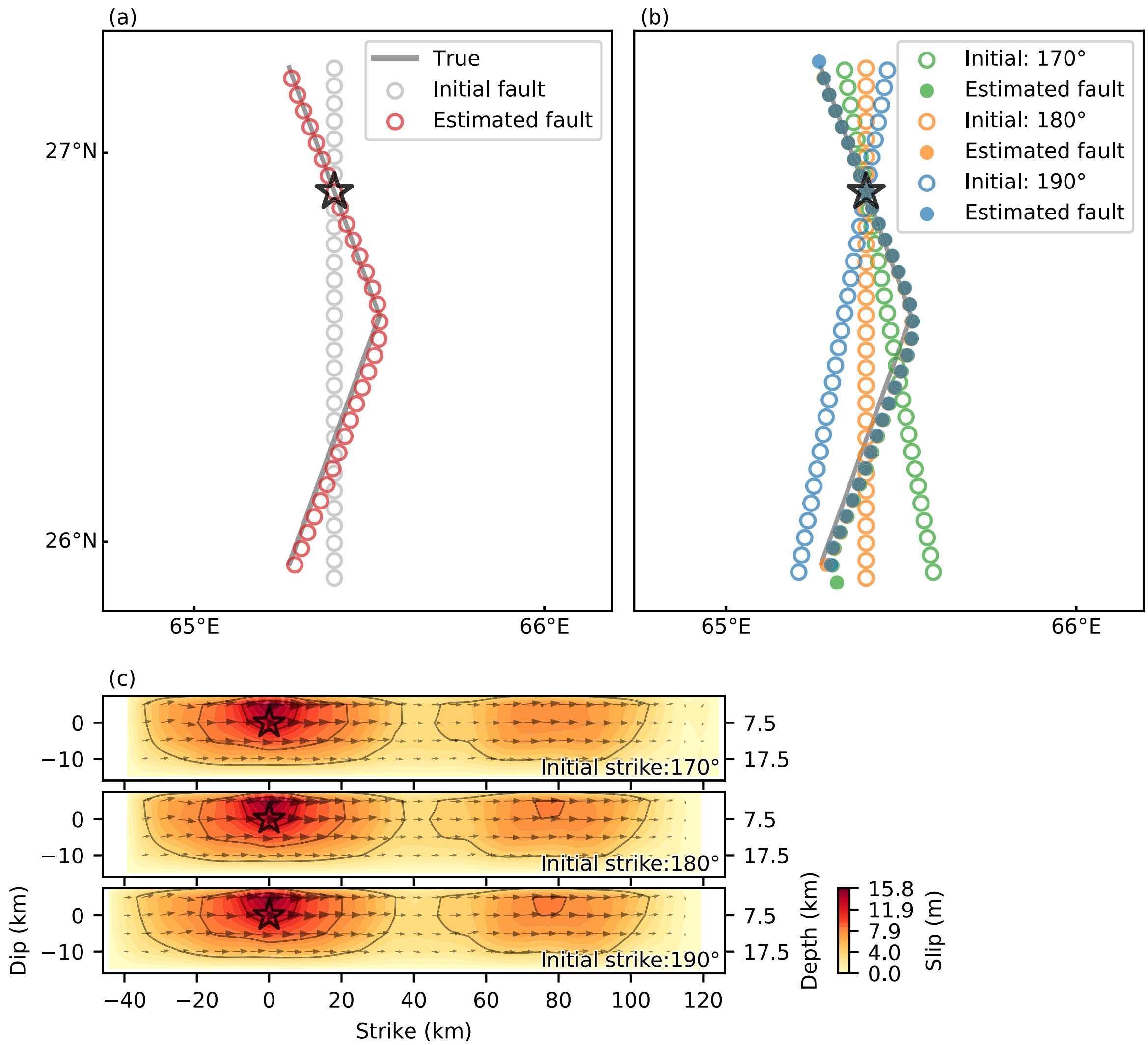

Figure 3. Results of synthetic test case 1. (a) True, initial, and estimated fault traces. The grey line represents the trace of the true fault surface. Grey and red circles represent the central points of subfaults of the initial and estimated model fault surfaces, respectively. The star denotes the epicentre. (b) Sensitivity of results to the strike of the initial model fault plane. All three initial fault planes (open circles) yield estimated fault traces (filled circles) that are nearly indistinguishable at the scale of this plot. (c) Estimated slip distribution on the model fault surface; contour interval is 4 m. The arrows represent slip vectors.

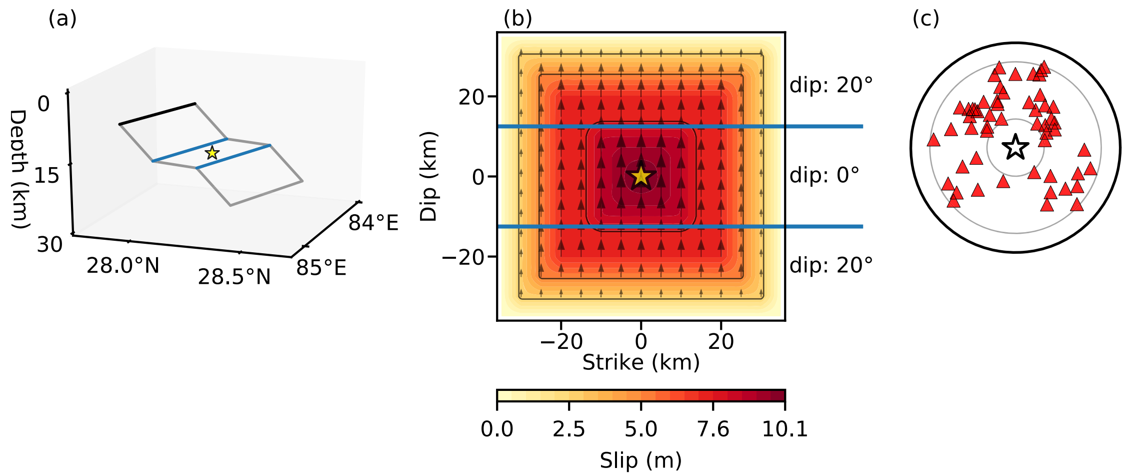

Figure 4. Input source model for case 2. (a) Fault geometry. The input fault plane consists of three rectangles with a ramp-flat-ramp structure. Black and blue lines are top of model fault and intersections of subplanes, respectively. The yellow star denotes the hypocentre. (b) Slip distribution on the input fault plane; contour interval is 2.5 m. The arrows represent slip vectors. (c) Station distribution (red triangles) around the epicentre (star) in an azimuthal equidistant projection. The grey circles indicate the 30° and 90° teleseismic distances.

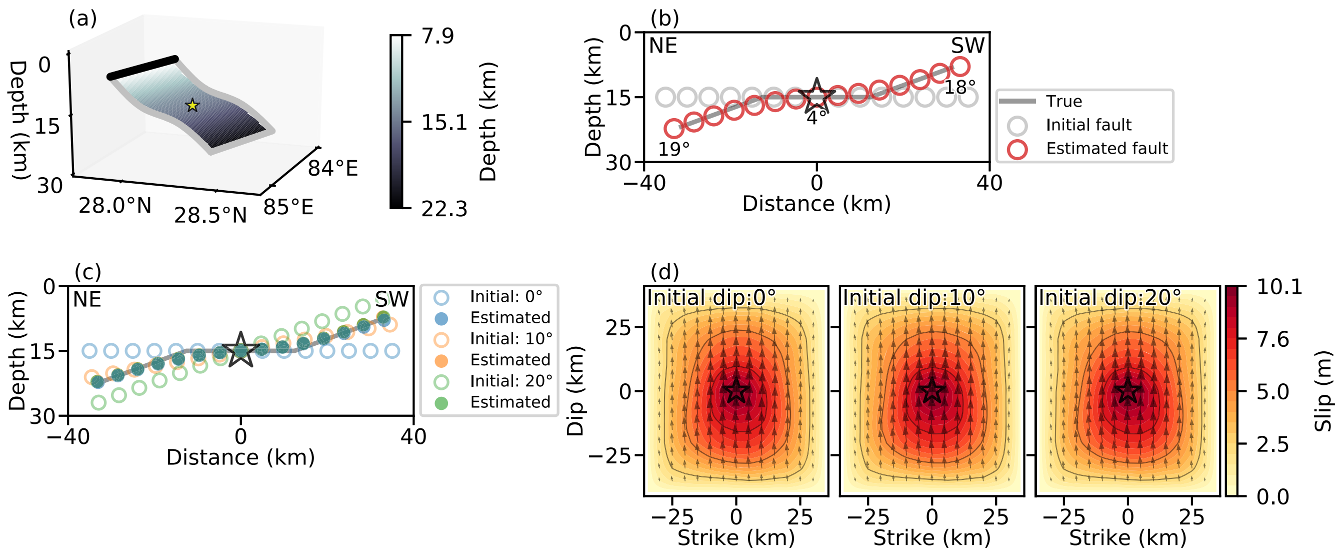

Figure 5. Results of synthetic test case 2. (a) Estimated fault geometry. The star denotes the hypocentre. (b) Cross sections of the true, initial, and estimated fault surfaces. (c) Sensitivity of results to the dip of the initial fault plane. All three initial fault planes (open circles) yield estimated fault traces (filled circles) that are indistinguishable at the scale of this plot. (d) Estimated slip distribution on the model fault surface; contour interval is 2.5 m. The arrows represent slip vectors.

d). These results confirm that the proposed method works well for faults with bending along dip.

4 APPLICATION TO REAL WAVEFORMS

In order to further examine the validity of the proposed method, we applied it to the M_W 7.7 2013 Balochistan, Pakistan, and the M_W 7.9 2015 Gorkha, Nepal, earthquakes. Fault geometries of the both earthquakes have been well constrained by previous studies showing that they occurred on non-planar faults. Thus, these earthquakes provide us opportunities to test whether the proposed method can reconstruct curved fault geometries.

4.1 The 2013 Balochistan earthquake

The Balochistan earthquake was a strike-slip event as indicated by Global Centroid Moment Tensor (GCMT; Dziewonski *et al.* 1981; Ekström *et al.* 2012,https://www.globalcmt.org/CMTsearch.html; last accessed 17 January 2020) solution and the *W*-phase moment tensor solution determined by the U.S. Geological Survey, National Earthquake Information Center (USGS NEIC; https://earthquake.usgs.gov/earthquakes/eventpage/usb000jyiv, last accessed 17 January 2020). Analyses of optical satellite images acquired after the earthquake (Avouac *et al.* 2014; Jolivet *et al.* 2014; Zinke *et al.* 2014) showed surface displacements that describe a curve convex to the south-east. The teleseismic *P*-waveform inversion analysis of Shimizu *et al.* (2020) yielded a source model suggesting strike-slip faulting in which the strike rotates from 205° at the north end to 240° at the south end.

Our inversion analysis used the observed vertical components of teleseismic *P* waveforms converted to velocity (Supporting Information Fig. S1) at 36 stations shown in Fig. 2(c), the same data used by Shimizu *et al.* (2020), and then resampled the waveform data at 0.8 s intervals without applying any filter. We adopted the USGS epicentre of 26.900°N, 65.400°E and the hypocentral depth of 7.5 km used by Shimizu *et al.* (2020). Theoretical Green's functions were calculated the same way as the synthetic tests in Section 3, using the 1-D near-source velocity structure (Supporting Information Table. S1) used in Avouac *et al.* (2014). The initial fault plane was 200 km long and 20 km wide, with a strike of 230° and a dip of 90°, that roughly followed the trace of the surface rupture observed by Zinke *et al.* (2014) (Fig. 6a). The potency rate density functions on this plane were expanded by bilinear B-spline functions with a spatial interval of 5 km and by linear B-spline functions with a temporal interval of 0.8 s and a total duration of 31 s. We also assumed the maximum rupture-front velocity to be 4 km s^{-1} and the potency rate density to be zero after 60 s from the rupture initiation, following the finite-fault inversion analysis of Shimizu *et al.* (2020). We adopted a plane with a strike of 226° and a dip of 69°, derived from the total potency tensor obtained by a preliminary analysis, as the reference surface used for selecting realistic nodal planes.

The inversion results after the third iteration, shown in Fig. 6, had an excellent fit between the observed and synthetic waveforms at all stations (Supporting Information Fig. S1). We defined a variance reduction to quantify the fit:

$$\text{Variance Reduction (per cent)} = \left(1 - \frac{\sum_j \sum_t \left(u_j^{obs}(t) - u_j^{syn}(t)\right)^2}{\sum_j \sum_t u_j^{obs}(t)^2}\right) \times 100, \tag{5}$$

where u_j^{obs} and u_j^{syn} represent observed and synthetic waveforms obtained by the inversion analysis at the *j*th station at time *t*, and our source model of the Balochistan earthquake yielded a variance reduction of 69.3 per cent. The estimated fault trace is 205 km long and curved, with a strike that changes from 218° at the northern edge around 50 km north-east of the epicentre, to 213° around the epicentre, to 241° at the southern edge around 140 km south-west of the epicentre (Fig. 6a). Its geometry is consistent with the surface ruptures observed after the earthquake (e.g. Zinke *et al.* 2014), shown by the grey line in Fig. 6(a), though the estimated fault geometry is slightly smoother than the observed surface rupture trace, which is possibly originated from our methodology, in which the dip angle is given to be uniform along the fault surface. Focal mechanisms along the fault trace (Fig. 6a), obtained by integrating the potency density tensors (Fig. 6b) along the dip direction, clearly show that strike-slip faulting is dominant. Integrating the potency density tensors (Fig. 6b) over the model fault surface yields the total potency tensor of this earthquake (Fig. 6a), which indicates strike-slip faulting with a strike of 226° and a dip of 69°. The total seismic moment release is 6.16 × 10 Nm (M_W 7.8), which is comparable to the estimate of 7.53 × 10^{20} Nm (M_W 7.8) by Shimizu *et al.* (2020) and the GCMT solution of 5.59 × 10^{20} Nm (M_W 7.8). The estimated source-time function, with a prominent peak at around 12 s and three minor peaks at around 28, 43, and 58 s (Fig. 6a), is comparable to the result of Shimizu *et al.* (2020).

Although focal mechanisms have two nodal planes, we could select the realistic fault plane from the focal mechanisms obtained in this inversion analysis by using the reference surface (Figs 6a and b). Decomposing the potency density tensors at the Earth's surface into the strike-slip component (positive for left-lateral fault slip) and the dip-slip component (positive for reverse fault slip), as shown in Fig. 6(c), demonstrates that left-lateral strike-slip is predominant, reaching a maximum of 16.3 m near the epicentre and gradual decrease towards both ends of the fault. The dip-slip component has a maximum value of 3.0 m at a point 25 km north-east of the epicentre and decreases to −1.3 m (1.3 m normal faulting) at a point 100 km south-west of the epicentre with small fluctuation (Fig. 6c).

Dip angles, which were derived from the realistic fault planes selected from the obtained focal mechanisms on the fault surface, range from 57° to 89° (Fig. 6d). Dip is recognizably dependent on depth, being steeper in the shallower part of the fault surface consistent with the idea of a listric fault, especially around the epicentre and 100 km south-west of the epicentre (Fig. 6d). Around the epicentre, the dip gradually increases from 68° at 17.5 km depth to 72° at 2.5 km depth (Fig. 6d). Around 100 km south-west of the epicentre, the depth dependence of the dip angle is clearer than that around the epicentre; the dip angle increases from 60° at 17.5 km depth to 71° at 2.5 km depth (Fig. 6d).

4.2 The 2015 Gorkha earthquake

Both the GCMT solution (Dziewonski *et al.* 1981; Ekström *et al.* 2012) and the *W*-phase moment tensor solution determined by the USGS NEIC (https://earthquake.usgs.gov/earthquakes/eventpage/us20002926, last accessed 17 January 2020) indicate that the Gorkha earthquake was a thrust event with a fault surface dipping at 7°. A teleseismic *P*-waveform inversion analysis (Yagi & Okuwaki 2015) produced a finite-fault source model in which the main rupture area is distributed around 50 km east of the epicentre. The Gorkha earthquake has been reported to have occurred along the Main Himalayan Thrust (e.g. Avouac *et al.* 2015; Duputel *et al.* 2016; Elliott *et al.* 2016; Hubbard *et al.* 2016). An analysis of Interferometric Synthetic Aperture Radar (InSAR) and Global Navigation Satellite System (GNSS) data (Elliott *et al.* 2016) showed that the earthquake occurred on a north-dipping fault with a ramp-flat-ramp structure, dipping at 30° from the surface to 5 km depth, 7° in a relatively flat section 75 km wide, and 20° in the deepest section 30 km wide. Hubbard *et al.* (2016) proposed a similar geometric model of the Main Himalayan Thrust, covering the source area of the Gorkha earthquake, on the basis of geological data in which the central portion had a 7° dip and the adjoining portions on the up-dip and down-dip sides had a 26° dip. Duputel *et al.* (2016) also proposed a ramp-flat-ramp fault geometry for the Gorkha earthquake on the basis of a receiver function analysis.

Our inversion analysis used the observed vertical components of teleseismic *P* waveforms converted to velocity (Supporting Information Fig. S2) at the 54 stations shown in Fig. 4(c), the same data used by Yagi & Okuwaki (2015), and then resampled the waveform data at 1.0 s intervals without applying any filter. We adopted the USGS epicentre of 28.231°N, 84.731°E and the hypocentral depth of 15 km used by Yagi & Okuwaki (2015). Theoretical Green's functions were calculated the same way as the synthetic tests in Section 3, using the 1-D near-source velocity structure (Supporting Information Table. S2) from the CRUST 1.0 model (Laske *et al.* 2013). The initial fault plane was 160 km long and 110 km wide, with a strike of 285° and a dip of 0°, that entirely covered the possible source region estimated by Yagi & Okuwaki (2015) (Fig. 7a). The potency rate density functions on the model fault plane were expanded by bilinear B-spline functions with a spatial interval of

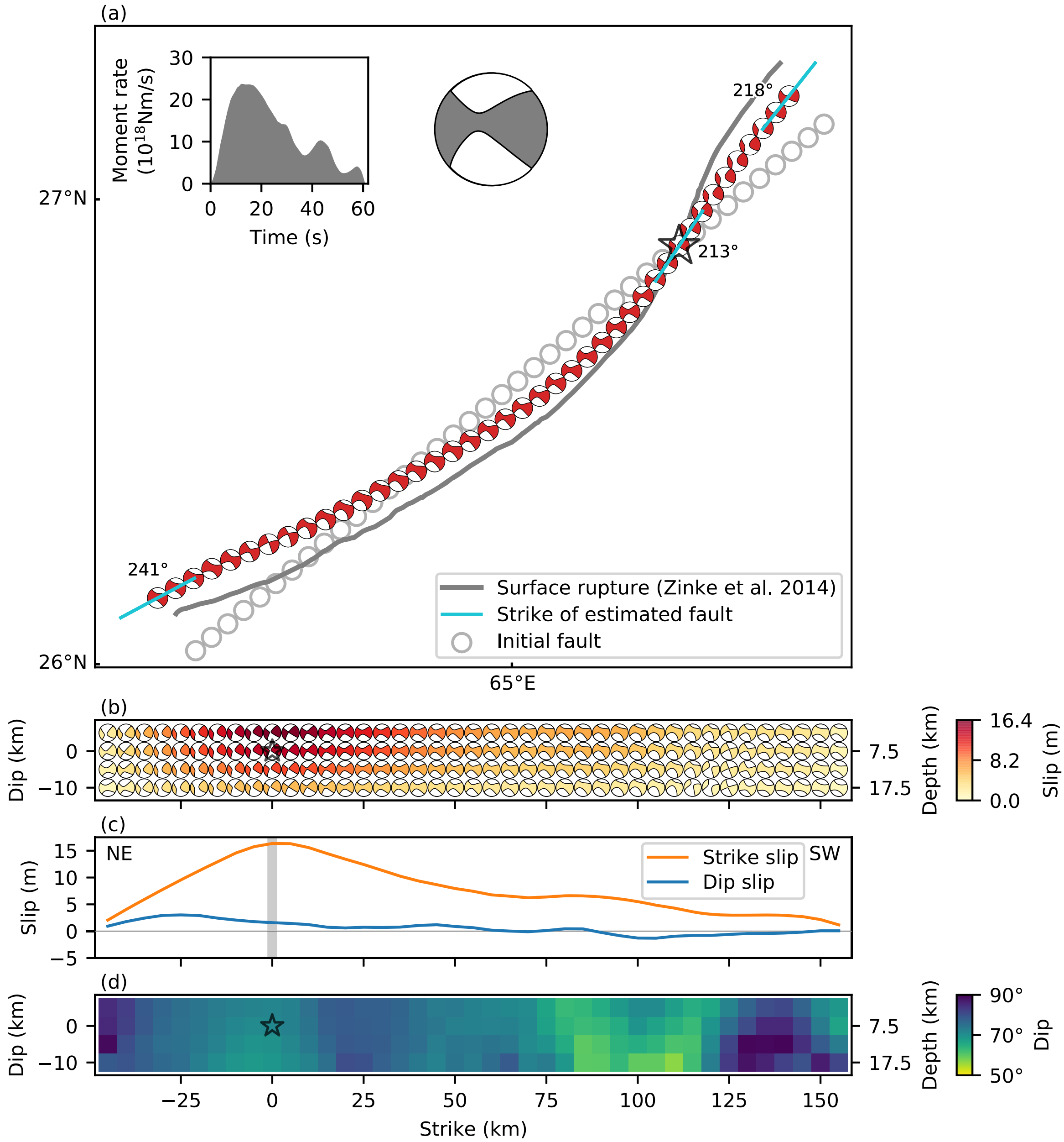

Figure 6. Source model of the 2013 Balochistan earthquake estimated by the proposed method. (a) The initial fault geometry is shown by grey circles at the centre of subfaults. The small beachball symbols show the focal mechanisms of the subfaults on the estimated fault trace, obtained by integrating the potency density tensors, shown in (b), with respect to the dip direction. Blue bars and numbers indicate the strike of the subfaults at the hypocentre and both ends of the estimated fault. The large beachball symbol shows the total potency tensor of the earthquake, obtained by integrating the potency density tensors shown in (b), over the fault surface. The grey line represents the surface rupture trace observed by Zinke *et al.* (2014). The inset shows the estimated moment rate function of the earthquake. The star denotes the epicentre. (b) Distribution of potency density tensors on the estimated fault surface. Beachball symbols indicate the focal mechanism at each subfault and their colour indicates the slip amount. (c) Profiles along the model fault trace of the strike-slip and dip-slip components, estimated from the potency density tensors at the top of the fault surface. The strike-slip component is positive for left-lateral faulting, and the dip-slip component is positive for reverse faulting. The grey vertical bar represents the location of the epicentre. (d) Distribution of dip (colour) on the estimated fault surface.

10 km and 5 km along the strike and dip directions, respectively, and by linear B-spline functions with a temporal interval of 1.0 s and a total duration of 28 s. We also assumed the maximum rupture-front velocity to be 3 km s^{-1} and the potency rate density to be zero after 60 s from the rupture initiation, following Yagi & Okuwaki (2015). We adopted a plane with a strike of 326° and a dip of 8°, derived from the total potency tensor obtained by a preliminary analysis, as the reference surface used for selecting realistic nodal planes.

The inversion results after the third iteration, shown in Fig. 7, had an excellent fit between the observed and synthetic waveforms (Supporting Information Fig. S2) and yielded a variance reduction (eq. 5) of 82.1 per cent. The fault plane dips towards the north-east and is 105 km wide (Fig. 7b). The spatial distribution of potency density tensors (Fig. 7a) shows that the main rupture area (>50 per cent of the maximum slip) is distributed around 50 km east of the epicentre, where the maximum slip is 5.0 m. The main rupture

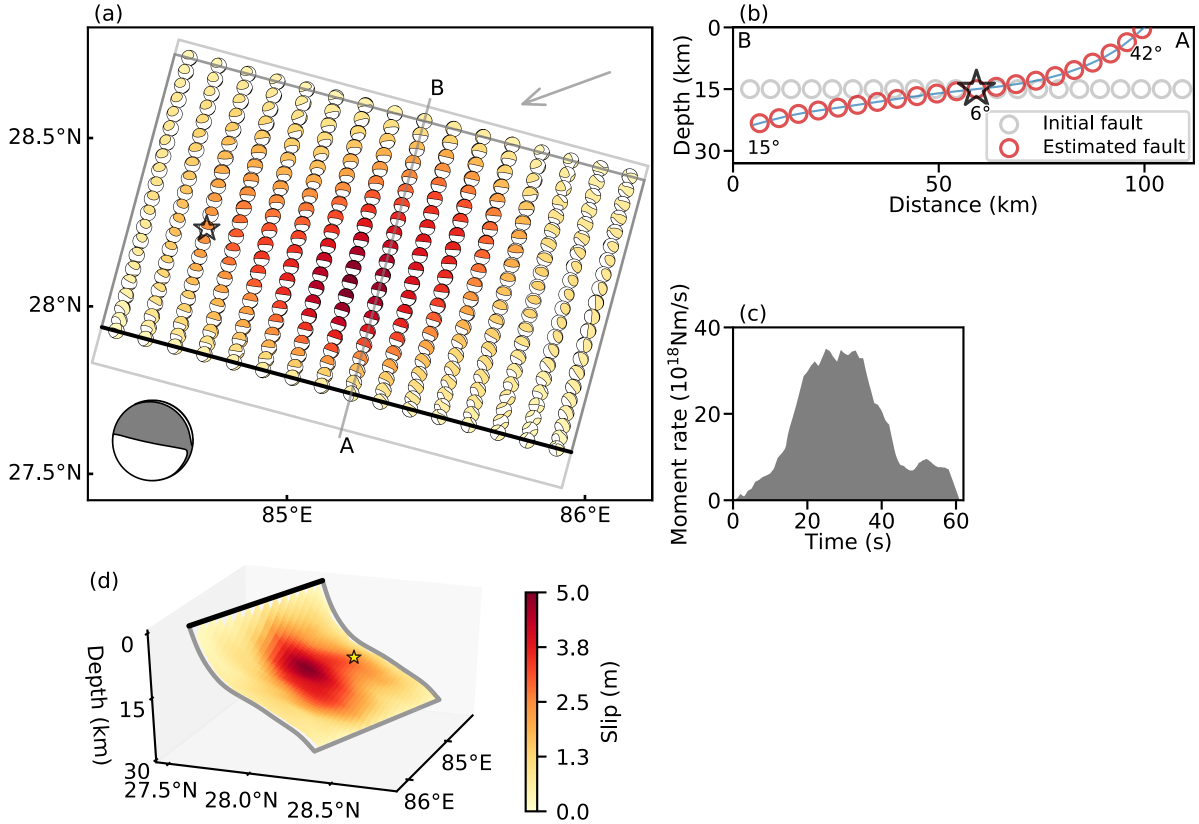

Figure 7. Source model of the 2015 Gorkha earthquake estimated by the proposed method. (a) Distribution of potency density tensors on the estimated fault surface. The light grey line outlines the initial fault plane. Small beachball symbols indicate the focal mechanism for each subfault and their colour indicates the slip amount according to the colour scale in (d). The large beachball symbol shows the total potency tensor of the earthquake, obtained by integrating the potency density tensors over the fault surface. Arrow indicates azimuth of 3-D view of (d). (b) Cross section of the model-fault surface along line A–B in (a). Grey and red circles represent the central points of subfaults of the initial and estimated model fault surfaces, respectively. Blue bar indicates the dip of each subfault. Denoted numbers are dip angles at the hypocentre and both ends of the estimated fault. (c) Estimated moment rate function of the earthquake. (d) Estimated fault geometry and slip amount (colour) viewed from the north-east indicated by the arrow in (a).

area is dominated by thrust faulting with dips ranging from 2° to 22°. The total potency tensor indicates thrust faulting with a strike of 332° and a dip of 9° (Fig. 7a). The total seismic moment release is 9.1×10^{20} Nm (M_W 7.9), which matches the 9.1×10^{20} Nm (M_W 7.9) estimated by Yagi & Okuwaki (2015). The cross section of the estimated fault surface (Fig. 7b), taken perpendicular to the fault strike (the A−B line shown in Fig. 7a), shows that the dip changes from 42° at the up-dip edge (45 km south-west of the hypocentre) to a minimum of 6° at the hypocentre to 15° at the down-dip edge (55 km north-east of the hypocentre). As seen in the 3-D view of the fault model (Fig. 7d), we resolved the main rupture area distributed in the flat part of the model fault surface with lower dip (<10°). Both the up- and down-dip part of the main rupture area were bounded by the ramp structure with higher dip angles.

5 DISCUSSION

In this study, we proposed a nonlinear inversion method to construct the fault geometry of an earthquake through the development of the finite-fault inversion method of Shimizu *et al.* (2020). They estimated spatial distribution of potency density tensors on an assumed fault plane, from which we can extract information on slip direction on the fault plane. Through synthetic tests and application to real waveform data, we showed that our proposed method can construct the fault geometry well, even if the strike or dip varies along the fault surface. Thus, it is possible to directly compare the obtained source model with other observed data, as can be done for source models obtained by using conventional inversion methods.

The clear surface ruptures from the Balochistan earthquake documented by Zinke *et al.* (2014) can be readily compared with our source model (Fig. 6a) and seen to be in good agreement. The increased surface displacement around the hypocentre in our model (Fig. 6b) is also consistent with the distribution of surface displacement across the fault trace estimated by the analyses of optical satellite images (e.g. Avouac *et al.* 2014; Zinke *et al.* 2014) and the slip distribution of finite-fault model of Avouac *et al.* (2014) (Supporting Information Figs S3a and b). The Arabia plate subducts beneath the Eurasia plate in the southern part of the Makran accretionary wedge, and active thrust faults exist in the Makran accretionary wedge (Haghipour *et al.* 2012), the site of the Balochistan earthquake hypocentre. The shallowing dip with increasing depth on the estimated fault surface (Fig. 6d) may suggest that the earthquake ruptured a thrust fault that has listric geometry. The dip angle in our fault model shows steeper at around the epicentre and shallower at around 100 km south-west from the epicentre (Fig. 6d), but the along-strike variation of dip angle seems not to be continuous and generally steeper than those in the models of Avouac *et al.* (2014) (Supporting Information Fig. S3c) and Jolivet *et al.* (2014). Although our model itself may represent a listric geometry of the Balochistan earthquake as discussed in Avouac *et al.* (2014)

and Jolivet *et al.* (2014), it should be difficult to judge whether Avouac *et al.* (2014)'s or Jolivet *et al.* (2014)'s model would be more consistent with our model.

Because the Gorkha earthquake did not produce surface ruptures (e.g. Avouac *et al.* 2015), there are no observational data that can be directly compared with our estimated fault geometry. Our source model of the Gorkha earthquake has a fault geometry with a ramp-flat-ramp structure (Figs 7b and d and Supporting Information Fig. S4), which is consistent with the fault geometry modelled by using geophysical and geological data (e.g. Elliott *et al.* 2016; Hubbard *et al.* 2016; Duputel *et al.* 2016), although the flat part is narrower in our model. In particular, the ramp structures in the up- and down-dip parts of our fault model can be considered to represent the middle and the deep ramps of the Main Himalayan Thrust model presented by Hubbard *et al.* (2016). The estimated slip distribution, with larger slip in the flat part (Figs 7a and d and Supporting Information Fig. S4), is also consistent with the analysis of InSAR and GNSS data by Elliott *et al.* (2016). The fault geometry modelled by Hubbard *et al.* (2016), using geological knowledge and the slip distribution estimated by Avouac *et al.* (2015), also places the main rupture area in the flat part of the fault. The dip angles of the ramp structures in the up- and down-dip parts of our fault model are different from those of the fault geometry modelled by Hubbard *et al.* (2016), but our source model can be considered to resolve the main rupture area bounded by the ramp structures, which is consistent with the model of Hubbard *et al.* (2016). Therefore, our proposed method, based solely on teleseismic data, yields a source model of the Gorkha earthquake that is comparable to fault geometry and slip distributions independently estimated from geophysical and structural geology data.

Because our proposed method uses spline interpolation in constructing fault geometry, continuous and geometrically smooth faults are best suited to this method. Furthermore, a realistic strike or dip was selected for each subfault on the basis of the similarity of the resolved nodal plane to the single reference surface. This procedure implicitly assumes that the strike or dip varies by less than 45° because a rotation of a focal mechanism around its own *B* axis greater than 45° places the conjugate nodal plane closer to the reference surface. This assumption was sound in the cases the Balochistan and Gorkha earthquakes because the strike and dip of their faults varied by less than 45°. Our proposed method may be extended to construct a fault geometry with a greater variation of strike or dip than 45° by determining a realistic nodal plane on the basis of the nodal plane of the adjacent subfault and extending this procedure sequentially in the direction away from the epicentre. Unlikely to inversion methods of geodetic data, our proposed method can estimate rupture process as well as fault geometry and would be applicable to an earthquake occurred under seafloors with poor geodetic observations. On the other hand, it would be difficult to use our proposed method to construct a conjugated fault system or a segmented fault system, such as the faults of the M_W 7.8 2016 Kaikoura, New Zealand, and the M_W 7.9 2018 Alaska earthquakes.

Our proposed method is optimized for application to teleseismic *P* waveform data because modelling error of teleseismic *P*-wave Green's function is well defined in the inversion method used in this study (Shimizu *et al.* 2020). It would be possible to jointly use teleseismic *S* waveforms and geodetic data by considering possible errors of picking first motion of *S*-phase and modelling error of geodetic Green's function. The spatial resolution of the fault geometry constructed by our proposed method is limited by the product of the sampling interval of waveform data and the assumed maximum rupture front velocity, but may be lower due to the smoothing constraints adopted by the inversion method of Shimizu *et al.* (2020). The joint use of geodetic data would make it possible to increase the spatial resolution and to constrain the absolute location of the constructed fault geometry. The smoothing constraints also impose CLVD components on potency density tensors estimated by the inversion method of Shimizu *et al.* (2020), even when a true source mechanism is pure double couple. Thus, it is difficult for the inversion method of Shimizu *et al.* (2020) to constrain the strike of low angle thrust fault, such as that of the Gorkha earthquake, which makes it difficult to use strike angles to construct fault geometry of such low angle thrust by using our proposed method and was the reason why we used only dip angles to construct the fault geometry of the Gorkha earthquake.

In each application of our method to both synthetic and real waveforms, it took only a few iterations of the finite-fault inversion to reconstruct the fault geometry, which was expected from the assumption that the fault geometry can be constructed from strike or dip data alone. Although this assumption results in a weak nonlinearity in our method, nonlinearities may also stem from the low spatial resolution of teleseismic data and the fact that the uncertainty of the Green's function is taken into account in the finite-fault inversion (Shimizu *et al.* 2020).

6 CONCLUSIONS

We proposed and tested a method of constructing fault geometry that relies on only teleseismic data, using a finite-fault inversion iteratively to estimate potency density tensor distributions that can express slips in an arbitrary direction. We assumed that an estimated fault surface has bends only along the strike or only in the dip direction, which leads to a weak nonlinearity of the method. After testing the performance of the method through synthetic tests, we applied this method to the 2013 Balochistan and 2015 Gorkha earthquakes, which previous studies have shown to have occurred along geometrically complex fault systems. For both events, our estimates of the fault geometry were consistent with previous studies that analysed different observational data. This method works well for constructing the fault geometry of an earthquake that ruptured a geometrically smooth and continuous fault surface.

ACKNOWLEDGEMENTS

We thank the editor Andrea Morelli, the reviewer Jean-Philippe Avouac and the anonymous reviewer for their thorough and constructive reviews that significantly improved our manuscript. This work was supported by Grant-in-Aid for Scientific Research (JP19K04030) and Grants-in-Aid for Scientific Research on Innovative Areas (JP16H06477, JP18H05447). The authors thank Keita Kayano for his valuable comments and suggestions during the early stage of this study. Teleseismic waveforms from the networks, GEOSCOPE, Hong Kong Seismographic Network, Global Telemetered Seismograph Network (USAF/USGS), New China Digital Seismograph Network, Global Seismograph Network (GSN-IRIS/IDA), Global Seismograph Network (GSN-IRIS/USGS), the Canadian National Seismograph Network, Czech Regional Seismic Network, GEOFON, the MEDNET Project, Pacific21, and the United States National Seismic Network, were downloaded from the IRIS-DMC website (https://ds.iris.edu/ds/nodes/dmc/). All the figures were created with matplotlib (Hunter 2007, Version 3.2.1; https://doi.org/10.5281/zenodo.3714460) and ObsPy

(Krischer *et al.* 2015; Megies *et al.* 2011; Beyreuther *et al.* 2010, Version 1.2.1; http://doi.org/10.5281/zenodo.3706479).

REFERENCES

Aki, K., 1979. Characterization of barriers on an earthquake fault, *J. geophys. Res.,* **84**(B11), 6140–6148.

Ampuero, J.P. & Dahlen, F.A., 2005. Ambiguity of the moment tensor, *Bull. seism. Soc. Am.,* **95**(2), 390–400.

Asano, K. & Iwata, T., 2009. Kinematic source inversion using strong motion data considering three-dimensional fault geometry, in *AGU Fall Meeting Abstracts,* Vol. **2009,** AGU, pp. S31A–1688.

Avouac, J.P., *et al.*, 2014. The 2013, Mw 7.7 Balochistan earthquake, energetic strike-slip reactivation of a thrust fault, *Earth planet. Sci. Lett.,* **391,** 128–134.

Avouac, J.-P., Meng, L., Wei, S., Wang, T. & Ampuero, J.-P., 2015. Lower edge of locked Main Himalayan Thrust unzipped by the 2015 Gorkha earthquake, *Nat. Geosci.,* **8**(9), 708–711.

Beyreuther, M., Barsch, R., Krischer, L., Megies, T., Behr, Y. & Wassermann, J., 2010. ObsPy: a Python toolbox for seismology, *Seismol. Res. Lett.,* **81**(3), 530–533.

Dal Zilio, L., van Dinther, Y., Gerya, T. & Avouac, J.-P., 2019. Bimodal seismicity in the Himalaya controlled by fault friction and geometry, *Nat. Commun.,* **10**(1), 48.

Duputel, Z. & Rivera, L., 2017. Long-period analysis of the 2016 Kaikoura earthquake, *Phys. Earth planet. Inter.,* **265,** 62–66.

Duputel, Z., Kanamori, H., Tsai, V.C., Rivera, L., Meng, L., Ampuero, J.P. & Stock, J.M., 2012a. The 2012 Sumatra great earthquake sequence, *Earth planet. Sci. Lett.,* **351–352,** 247–257.

Duputel, Z., Rivera, L., Kanamori, H. & Hayes, G., 2012b. W phase source inversion for moderate to large earthquakes (1990-2010), *Geophys. J. Int.,* **189**(2), 1125–1147.

Duputel, Z., Vergne, J., Rivera, L., Wittlinger, G., Farra, V. & Hetényi, G., 2016. The 2015 Gorkha earthquake: a large event illuminating the Main Himalayan Thrust fault, *Geophys. Res. Lett.,* **43**(6), 2517–2525.

Dziewonski, A.M., Chou, T. & Woodhouse, J., 1981. Determination of earthquake source parameters from waveform data for studies of global and regional seismicity, *J. geophys. Res.,* **86**(B4), 2825–2852.

Ekström, G., Nettles, M. & Dziewoński, A.M., 2012. The global CMT project 2004–2010: centroid-moment tensors for 13,017 earthquakes, *Phys. Earth planet. Inter.,* **200-201,** 1–9.

Elliott, J.R., Jolivet, R., Gonzalez, P.J., Avouac, J.P., Hollingsworth, J., Searle, M.P. & Stevens, V.L., 2016. Himalayan megathrust geometry and relation to topography revealed by the Gorkha earthquake, *Nature Geoscience,* **9**(2), 174–180.

Fielding, E.J., Sladen, A., Li, Z., Avouac, J.P., Bürgmann, R. & Ryder, I., 2013. Kinematic fault slip evolution source models of the 2008 M7.9 wenchuan earthquake in china from SAR interferometry, GPS and teleseismic analysis and implications for longmen shan tectonics, *Geophys. J. Int.,* **194**(2), 1138–1166.

Fukahata, Y. & Wright, T.J., 2008. A non-linear geodetic data inversion using ABIC for slip distribution on a fault with an unknown dip angle, *Geophys. J. Int.,* **173**(2), 353–364.

Haghipour, N., Burg, J.P., Kober, F., Zeilinger, G., Ivy-Ochs, S., Kubik, P.W. & Faridi, M., 2012. Rate of crustal shortening and non-Coulomb behaviour of an active accretionary wedge: the folded fluvial terraces in Makran (SE, Iran), *Earth planet. Sci. Lett.,* **355–356,** 187–198.

Hartzell, S.H. & Heaton, T.H., 1983. Inversion of strong ground motion and teleseismic waveform data for the fault rupture history of the 1979 Imperial Valley, California, earthquake, *Bull. seism. Soc. Am.,* **73**(6), 1553–1583.

Hubbard, J., Almeida, R., Foster, A., Sapkota, S.N., Bürgi, P. & Tapponnier, P., 2016. Structural segmentation controlled the 2015 MW 7.8 Gorkha earthquake rupture in Nepal, *Geology,* **44**(8), 639–642.

Hunter, J.D., 2007. Matplotlib: a 2D graphics environment, *Comput. Sci. Eng.,* **9**(3), 90–95.

Jolivet, R., *et al.*, 2014. The 2013 Mw7.7 Balochistan earthquake: Seismic potential of an accretionary wedge, *Bull. seism. Soc. Am.,* **104**(2), 1020–1030.

Kikuchi, M. & Kanamori, H., 1991. Inversion of complex body waves-III, *Bull. seism. Soc. Am.,* **81**(6), 2335–2350.

Krischer, L., Megies, T., Barsch, R., Beyreuther, M., Lecocq, T., Caudron, C. & Wassermann, J., 2015. ObsPy: a bridge for seismology into the scientific Python ecosystem, *Comput. Sci. Discov.,* **8**(1), 14003.

Laske, G., Masters, G., Ma, Z. & Pasyanos, M., 2013. Update on CRUST1.0—a 1-degree global model of Earth's crust, *EGU General Assembly 2013,* **15,** 2658.

Megies, T., Beyreuther, M., Barsch, R., Krischer, L. & Wassermann, J., 2011. ObsPy – what can it do for data centers and observatories?, *Ann. Geophys.,* **54**(1), 47–58.

Okuwaki, R. & Yagi, Y., 2018. Role of geometric barriers in irregular-rupture evolution during the 2008 Wenchuan earthquake, *Geophys. J. Int.,* **212**(3), 1657–1664.

Okuwaki, R., Hirano, S., Yagi, Y. & Shimizu, K., 2020. Inchworm-like source evolution through a geometrically complex fault fueled persistent supershear rupture during the 2018 Palu Indonesia earthquake, *Earth planet. Sci. Lett.,* **547,** 116449.

Olson, A.H. & Apsel, R.J., 1982. Finite faults and inverse theory with applications to the 1979 Imperial Valley earthquake, *Bull. seism. Soc. Am.,* **72**(6), 1969–2001.

Qiu, Q., *et al.*, 2016. The mechanism of partial rupture of a locked megathrust: the role of fault morphology, *Geology,* **44**(10), 875–878.

Ragon, T., Sladen, A. & Simons, M., 2018. Accounting for uncertain fault geometry in earthquake source inversions – I : theory and simplified application, *Geophys. J. Int.,* **214,** 1174–1190.

Shi, Q., Wei, S. & Chen, M., 2018. An MCMC multiple point sources inversion scheme and its application to the 2016 Kumamoto Mw 6.2 earthquake, *Geophys. J. Int.,* **215**(2), 737–752.

Shimizu, K., Yagi, Y., Okuwaki, R. & Fukahata, Y., 2020. Development of an inversion method to extract information on fault geometry from teleseismic data, *Geophys. J. Int.,* **220**(2), 1055–1065.

Wald, D.J. & Heaton, T.H., 1994. Spatial and temporal distribution of slip for the 1992 Landers, California, earthquake, *Bull. seism. Soc. Am.,* **84**(3), 668–691.

Yagi, Y. & Fukahata, Y., 2011. Introduction of uncertainty of Green's function into waveform inversion for seismic source processes, *Geophys. J. Int.,* **186**(2), 711–720.

Yagi, Y. & Okuwaki, R., 2015. Integrated seismic source model of the 2015 Gorkha, Nepal, earthquake, *Geophys. Res. Lett.,* **42**(15), 6229–6235.

Yue, H. & Lay, T., 2020. Resolving complicated faulting process using multi-point-source representation: iterative inversion algorithm improvement and application to recent complex earthquakes, *J. geophys. Res.,* **125**(2), 1–24.

Zinke, R., Hollingsworth, J. & Dolan, J.F., 2014. Surface slip and off-fault deformation patterns in the 2013 Mw7.7 Balochistan, Pakistan earthquake: implications for controls on the distribution of near-surface coseismic slip, *Geochem. Geophys. Geosyst.,* **15**(12), 5034–5050.

SUPPORTING INFORMATION

Supplementary data are available at *GJI* online.

Figure S1. Fitting between observed and synthetic waveforms of the Balochistan earthquake.

Figure S2. Fitting between observed and synthetic waveforms of the Gorkha earthquake.

Figure S3. Comparison with other studies of the Balochistan earthquake.

Figure S4. Comparison with another study of the Gorkha earthquake.

Figure S5. Potency density tensor distributions obtained after the first and the last iterations.

Table S1. Velocity structure in the source region of the 2013 Balochistan earthquake

Table S2. Velocity structure in the source region of the 2015 Gorkha earthquake

Please note: Oxford University Press is not responsible for the content or functionality of any supporting materials supplied by the authors. Any queries (other than missing material) should be directed to the corresponding author for the paper.